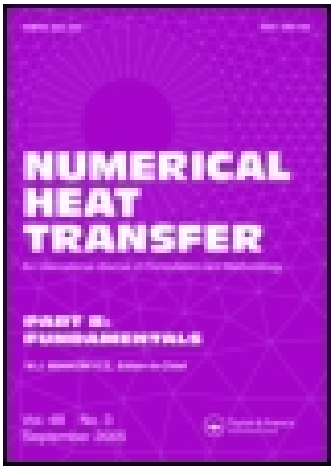

Numerical Heat Transfer, Part B: Fundamentals: An International Journal of Computation and Methodology

Publication details, including instructions for authors and subscription information:
http://www.tandfonline.com/loi/unhb20

Lattice Boltzmann Study of Bubble Dynamics

Ismail Oguz Kurtoglu [a] & Ching-Long Lin [a]

[a] Department of Mechanical and Industrial Engineering , IIHR—Hydroscience & Engineering, The University of Iowa , Iowa City, Iowa, USA

Published online: 24 Feb 2007.

To cite this article: Ismail Oguz Kurtoglu & Ching-Long Lin (2006) Lattice Boltzmann Study of Bubble Dynamics, Numerical Heat Transfer, Part B: Fundamentals: An International Journal of Computation and Methodology, 50:4, 333-351

To link to this article: http://dx.doi.org/10.1080/10407790500290659

Numerical Heat Transfer, Part B, 50: 333–351, 2006

ISSN: 1040-7790 print/1521-0626 online
DOI: 10.1080/10407790500290659

Taylor & Francis
Taylor & Francis Group

LATTICE BOLTZMANN STUDY OF BUBBLE DYNAMICS

Ismail Oguz Kurtoglu and Ching-Long Lin
Department of Mechanical and Industrial Engineering, IIHR—Hydroscience & Engineering, The University of Iowa, Iowa City, Iowa, USA

The purpose of this work is to assess the applicability of a new two-phase immiscible lattice Boltzmann method based on phase-field method to single bubble dynamics over a wide range of flow regimes. In two-dimensional domain, the bubble geometry, the interface deformation, and the bubble rise characteristics, such as terminal velocity, drag coefficient, and wake properties, are investigated and quantified using dimensionless parameters. These results are further verified by three-dimensional simulations. The results show an excellent agreement with those of the experimental studies and the level-set and volume-of-fluid numerical approaches.

1. INTRODUCTION

Gas–liquid systems are part of many natural physical processes, but more important, they are widely used in industry for various purposes. For example, gas is released into liquid phase to form small bubbles in boiling-water reactors for cooling the fusion core, in bubble column reactors for chemical reactions, and in boilers for producing steam. Consequently, the mass and heat transfer rates are maintained at a desired level by controlling bubble size or the interfacial area between one or more phases. In this respect, understanding of hydrodynamic properties of these multiphase reactors is crucial for designing purposes. However, complex interactions between gas and liquid phases make this problem quite challenging.

While the level-set method (LSM) and the volume-of-fluid method (VOF) coupled with the continuum Navier-Stokes equation solvers have been successfully applied to gas–liquid two-phase flow systems [1], the lattice Boltzmann method (LBM) is considered as an alternative approach to these methods due to its unique advantages, such as relatively easy coding and implementation in parallel computing, and its potential applications to gas microfluidic systems that exhibit velocity slip and rarefaction phenomena, without relying on *ad hoc* boundary conditions [2]. Fundamentals of the LBM are based on mesoscopic kinetic theories which lie between classical and molecular theories [3]. More recently, the Boltzmann equation has been expanded for general fluid behavior and has become a promising tool in the computational fluid dynamics (CFD) community [4].

Received 28 January 2005; accepted 27 May 2005.
Address correspondence to Ching-Long Lin, Department of Mechanical and Industrial Engineering, IIHR—Hydroscience & Engineering, The University of Iowa, Iowa City, IA 52242-1527, USA. E-mail: ching-long-lin@uiowa.edu

NOMENCLATURE

c	molecule's velocity
C	order parameter
C_D	drag coefficient
D	diameter
E_o	Eötvös number
f	distribution function
$f(\rho)$	free-energy density function
f^{eq}	equilibrium distribution function
$\mathbf{F}$	external force
g	distribution function
h	interface thickness
K_b, K_{b0}	parameters in the Fan and Tsuchiya terminal velocity equation
LBM	lattice Boltzmann model
LSM	level-set method
m	dimension of space
Mo	Morton number
n	parameter in the Fan and Tsuchiya terminal velocity equation
p	mechanic pressure
r	radius
R	universal gas constant
Re	Reynolds number
s	deviation from perfect sphericity
S	pressure-like scalar variable
T	temperature
$\mathbf{u}$	mean velocity of molecules
U_t	terminal velocity
VOF	volume of fluid
We	Weber number
$\mathbf{z}$	position vector
α	parameter in the free-energy density function
β	parameter in the free-energy density function
κ	free parameter
λ	relaxation time
μ	dynamic viscosity
μ_c	chemical potential
ν	kinematic viscosity
ρ	density
σ	surface tension
τ	relaxation parameter
Ψ	local excess free energy
Ω	collision function

Subscripts

e	equivalent
g	gas
l	liquid

Superscripts

eq	equilibrium state

Shan and Chen [5] presented a two-phase LBM model based on an interaction potential between fluids to overcome unphysical interfacial properties of the Rhotmann-Keller model [5], which relies on a color gradient to keep fluids separated. Nonetheless, the Shan-Chen model, like the Rothmann-Keller model, is computationally expensive. Besides, limitations in choosing effective density functions do not allow that model to simulate a wide variety of fluids. The search for a thermodynamically consistent model was continued by Swift, Osborn, and Yeomans [6]. Introducing an equilibrium pressure tensor in the collision term, they claimed that a correct thermodynamic equilibrium state based on the van der Waals free-energy density function had been reached. However, soon it was argued that since the free-energy approach did not satisfy the isothermal system assumption, it would not let the system reach a thermodynamically consistent state. Also, Holdych et al. [7] corrected the problem of the non-Galilean invariant property of this model.

In 1998, He et al. [8] presented a new model to overcome drawbacks found in the aforementioned models. Their idea was to adopt the lattice Boltzmann equation for dense fluids by including excluded volume effects. Similar study was also done by Luo [9] at about the same time. Later this model was successfully applied to simulate two-dimensional (2-D) and three-dimensional (3-D) Rayleigh-Taylor, and 2-D Kelvin-Helmholtz instabilities [10].

Several authors have applied LBMs to study bubble dynamics. For instance, Takada et al. [11] simulated single and two rising bubbles in a duct using Swift's LBM. Likewise, using Shan and Chen's model, Sankaranarayanan et al. [12] applied an implicit LBM to simulate rising bubbles. In this article, we describe a new phase-field LBM and apply it to single-bubble motion over a wide range of flow regimes. The current LBM is based on the phase-field method of Jacqmin [13], which is incorporated into the solution procedure for incompressible Navier-Stokes equations. Jacqmin demonstrated that the phase-field method is robust in simulating two-phase flows. Thus, the objectives of this article are twofold. The first objective is to present a phase-field LBM for two-phase flows. The second objective is to apply the LBM to single-bubble dynamics over a wide range of flow regimes and compare numerical solutions with existing experimental data as well as those computed from the LSM and VOF approaches for validation. The success of the phase-field LBM has the potential to extend it to microsystems so that the particulate nature of the LBM can be utilized in dealing with special types of boundary condition at micro-scale, such as wetting and nonwetting phenomena and velocity slip [2].

2. METHODOLOGIES

The traditional numerical solvers for binary immiscible fluid systems use two main approaches: sharp and diffuse interface methods. Sharp interface methods require solving the moving interface with appropriate boundary condition. However, interface tracking methods are inconvenient when interface breakage or coalescence occurs. On the other hand, in spite of low accuracy, diffuse interface methods are simpler and more flexible [14]. Jacqmin [13] proposed a diffuse interface phase-field method based on a fluid free-energy density function,

$$\phi = \frac{1}{2}\alpha|\nabla C|^2 + \beta\Psi(C) \tag{1}$$

where C is an order parameter that distinguishes the binary fluids and $\Psi(C)$ local excess free energy, which is minimum at the stable bulk phases. According to this formulation, the fluid's chemical potential, μ_c, is obtained by integration of the free-energy density function with respect to C. Hence

$$\mu_c = \beta\Psi'(C) - \alpha\nabla^2 C \tag{2}$$

Cahn and Hilliard theory [15] models the dynamics of diffuse interface, arguing that diffusion fluxes are proportional to the chemical potential gradient:

$$\frac{\partial C}{\partial t} = \kappa\nabla^2\mu_c = -\kappa\nabla^2[\alpha\nabla^2 C - \beta\Psi'(C)] \tag{3}$$

where κ is mobility. Therefore, the phase-field advection-diffusion equation for C is

$$\frac{\partial C}{\partial t} + \boldsymbol{u}\cdot\nabla C = \kappa\nabla^2\mu_c \tag{4}$$

In this equation, the term on the right-hand side is the antidiffusion term, which eliminates interfacial fluxes.

2.1. Two-Component Immiscible LBM

The phase-field advection equation for C is incorporated into the LBM framework through the nonideal LBM formulation of He et al. [8]:

$$\partial_t f + \boldsymbol{c} \cdot \nabla f = -\frac{(f - f^{\mathrm{eq}})}{\lambda} + \frac{(\boldsymbol{c} - \boldsymbol{u})}{\rho RT} \boldsymbol{F} f_{\mathrm{eq}} \tag{5}$$

where f is the particle distribution function, f^{eq} is the Maxwell-Boltzmann equilibrium distribution function, $\boldsymbol{c}$ is the microscopic velocity, $\boldsymbol{u}$ is the fluid velocity, ρ is the macroscopic fluid density, λ is the relaxation time due to particle collision, R is the gas constant, T is temperature, and the external force takes the form

$$\boldsymbol{F} = RT\nabla\rho - C\nabla\mu_c + \rho\boldsymbol{g} \tag{6}$$

Using the Chapman-Enskog expansion, the incompressible momentum equations can be obtained from Eq. (5):

$$\rho\frac{\partial \boldsymbol{u}}{\partial t} + \rho\boldsymbol{u} \cdot \nabla\boldsymbol{u} = -\nabla S + \mu\nabla^2\boldsymbol{u} - C\nabla\mu_c + \rho\boldsymbol{g} \tag{7}$$

where the scalar variable S is to satisfy incompressibility condition [13] and μ is viscosity, given by

$$\mu = \lambda\rho RT \tag{8}$$

Phase segregation in this model is realized by the intermolecular interaction force $\Psi(\rho)$. However, especially for high density ratios, this term may cause some instability problems because the gradient of this term is pretty large at the interface due to a density jump between the phases. He et al. [16] suggested a new variable to increase stability of the model. This variable reads

$$g = fRT + \psi(\rho)\Gamma(0) \tag{9}$$

where Γ is a function of the macroscopic velocity $\boldsymbol{u}$:

$$\Gamma(\boldsymbol{u}) = \frac{f^{\mathrm{eq}}}{\rho} = \frac{1}{(2\pi RT)^{m/2}} \exp\left[-\frac{(\boldsymbol{c} - \boldsymbol{u})^2}{2RT}\right] \tag{10}$$

where m is the dimension of the space. This transformation leads to the momentum transport equation,

$$\begin{aligned}\partial_t g + \boldsymbol{c} \cdot \nabla g = &-\frac{(g - g^{\mathrm{eq}})}{\lambda} + (\boldsymbol{c} - \boldsymbol{u}) \cdot \nabla\rho RT[\Gamma(\boldsymbol{u}) - \Gamma(0)] \\ &- (\boldsymbol{c} - \boldsymbol{u}) \cdot (\nabla S - \rho\boldsymbol{g} + C\nabla\mu)\Gamma(\boldsymbol{u}) + (\boldsymbol{c} - \boldsymbol{u}) \cdot \nabla S\Gamma(0)\end{aligned} \tag{11}$$

Therefore, the measure of phase, C, the incompressibility constraint, S, and the velocity, $\boldsymbol{u}$, can be calculated by taking moments of the distribution functions f and g,

$$C = \int f \, d\boldsymbol{c} \tag{12}$$

$$S = \int g \, d\boldsymbol{c} \tag{13}$$

$$\rho RT\boldsymbol{u} = \int \boldsymbol{c} g \, d\boldsymbol{c} \tag{14}$$

For numerical solution, Eqs. (5) and (10) are discretized over time and space using the Crank-Nicolson scheme [17].

2.2. Surface Tension and Interface Thickness

Since surface tension is excess free energy per unit surface area, it must be the function of density gradient across the interface. The van der Waals theory defines this relation for a flat interface via the equation

$$\sigma = \kappa \int_{-\infty}^{+\infty} [\rho'(z)]^2 \, dz \tag{15}$$

where z is the coordinate of the position vector. In order to calculate surface tension, the interface profile must be given. In the calculations, we use a profile defined for a flat interface:

$$\rho(z) = \frac{1}{2}(\rho_l + \rho_g) + \frac{1}{2}(\rho_l - \rho_g) \tanh\left(z \frac{\rho_l - \rho_g}{\sqrt{2\alpha/\beta}}\right) \tag{16}$$

where the subscripts l and g stand for liquid and gas, respectively.

Substitution of this interface profile into Eq. (15) leads to the interface thickness and the surface tension, which are

$$h = \frac{4}{\rho_l - \rho_g} \sqrt{\frac{\alpha}{2\beta}} \tag{17}$$

$$\sigma = \frac{(\rho_l - \rho_g)^3}{6} \sqrt{2\alpha\beta} \tag{18}$$

2.3. Computational Domain and Boundary Conditions

The 2-D simulations are performed in a computational domain size of 100×300. Initially, the center of a bubble with a diameter of 20 grid points is located at $x = 50$ and $y = 40$. No-slip boundary conditions are imposed at the bottom and

top walls of the domain. To keep the bubble motion away from wall effects, the periodic boundary condition is used at lateral boundaries of the domain. It is noted that the LBM requires substantial memory and computational efforts to resolve small-scale interface structures. For example, at a 2-D square lattice node there are 18 distribution functions: nine for density evaluation and nine for pressure evaluation. In addition, intermediate distribution functions used in the numerical algorithm double the memory need. A domain of 512×512 grid points consumes some 200 MB of memory with 13 CPU s/time step.

3. RESULTS AND DISCUSSION

Several important dimensionless parameters for characterizing bubble dynamics are defined below.

Eötvös (Bond) number:

$$\mathrm{Eo} = \frac{g \triangle \rho d_e^2}{\sigma} \tag{19}$$

Morton number:

$$\mathrm{Mo} = \frac{g\mu^4 \triangle \rho}{\rho^2 \sigma^3} \tag{20}$$

where d_e is the effective diameter, ρ is the density of continuous medium, and $\Delta\rho$ is the density difference between continuous and dispersed phases. Eo represents the dimensionless size of a bubble. Consequently, it determines the amount of deformation of the rising bubble. For instance, for small Eo (<1), the bubble is small and spherical because the surface tension is the deterministic force for its shape. Mo characterizes the properties of the liquid system surrounding a bubble. It has strong dependence on viscosity and surface tension.

The flow field around the bubble is determined by the Reynolds number, Re,

$$\mathrm{Re} = \frac{\rho d_e U_t}{\mu} \tag{21}$$

where U_t is bubble terminal velocity.

The Weber number, We, is related to the above dimensionless numbers by

$$\mathrm{We} = \frac{\rho_l U_t^2 d_e}{\sigma} = \mathrm{Re}^2 \sqrt{\frac{\mathrm{Mo}}{\mathrm{Eo}}} \tag{22}$$

Clift et al. [18] constructed a generalized regime map in terms of these numbers. The map has been widely used for prediction of terminal rise velocity and bubble shape for certain Eo and Mo numbers. It is known that at very small terminal velocities, bubbles or drops are spherical in shape. Surface tension and viscous forces

play more important roles in bubble dynamics than inertia forces do. Bubbles rise in a fluid under the effect of buoyancy forces without deforming. For this case, the bubble wake is laminar and does not create any trailing vortex structure. With increasing terminal velocity, inertia forces become effective. Dynamic pressure caused by the rising bubble acts against the motion triggered by hydrostatic pressure. Dynamic pressure decreases starting from the nose of the bubble to the sides of the bubble along the interface. Therefore, the bubble takes shapes such as ellipsoids or spherical caps. In addition to this deformation, the bubble wake becomes turbulent and vortices are formed in the wake region. Depending on surface tension, sometimes the bubble deforms so much that sharp edges at the sides of the bubble bend down, creating a skirtlike structure.

Any two-phase flow model is required to predict accurately bubble terminal velocity and bubble shape under differing flow conditions. In what follows, we examine bubble velocity and shape over a wide range of flow regimes to assess the applicability of the current phase-field LBM to bubble dynamics.

3.1. Bubble Rise Velocity

When a bubble is released in a stationary liquid, it moves freely in an upward direction under the influence of gravitational forces. We first assume that it reaches terminal condition where the drag, gravitational, and buoyant forces are in equilibrium. At this state, the bubble's terminal velocity is almost constant, and its shape can be assumed fixed.

For high Re, low Mo and Eo flows, after reaching a certain terminal velocity, the bubble leaves its linear trajectory, and its terminal velocity becomes erratic. Moreover, the bubble tends to change its major axis continuously, depending on its instantaneous motion. Because of this wobbling motion, terminal velocity cannot be used as a deterministic property and bubble shape cannot be predicted.

For sufficiently small spherical bubbles ($\mathrm{Re} < 1$), Stokes's solution can be used to estimate terminal velocity. For this case, viscous and capillary forces are dominant features:

$$U_t = \frac{g d_e^2}{18\nu} \tag{23}$$

When inertia forces become effective for bubbles in low-viscous liquids, Re is no longer small enough ($50 < \mathrm{Re} < 500$). Levic's theory may be applied for such cases:

$$U_t = \frac{g d_e^2}{36\nu} \tag{24}$$

When bubble size is sufficiently large, inertia forces become effective and bubble shape is flattened. For these cases, Mendelson suggested the following equation:

$$U_t = \sqrt{\frac{2\sigma}{\rho d_e} + \frac{g d_e}{2}} \tag{25}$$

Fan and Tsuchiya [19] combined Eqs. (23), (24), and (25) and suggested the following expression for spherical and ellipsoidal bubbles:

$$U_t\left(\frac{\rho_l}{\sigma g}\right)^{1/4} = \left[\left(\frac{\mathrm{Eo}}{K_b\,\mathrm{Mo}^{1/4}}\right)^{-n} + \left(\frac{2C_n}{\mathrm{Eo}^{1/2}} + \frac{\mathrm{Eo}^{1/2}}{2}\right)^{-n/2}\right]^{-1/n} \tag{26}$$

where n is a parameter in the range $0.8 < n < 1.6$ for purified to contaminated liquids. C_n is equal to 1.2 and 1.4 for monocomponent and multicomponent liquids, respectively. K_b is given by

$$K_b = K_{b0}\,\mathrm{Mo}^{-0.038} \qquad (K_b > 12) \tag{27}$$

where the value of K_{b0} is equal to 14.7 for water and 10.2 for organic solvents or mixtures. For liquids whose K_b is less than 12, K_b should be set to 12.

Using the theory of potential flow, Joseph [20] estimates the rise velocity for a spherical cap bubble by

$$\frac{U_t}{\sqrt{gd_e}} = -\frac{8}{3}\frac{\nu(1+8s)}{\sqrt{gd_e^3}} + \frac{\sqrt{2}}{3}\left[1 - 2s - \frac{16s\sigma}{\rho g d_e^2} + \frac{32\nu^2}{gd_e^3}(1+8s)^2\right]^{1/2} \tag{28}$$

where s is the deviation of the bubble nose from perfect sphericity. For instance, for $s < 0$ the bubble nose is pointed, for $s > 0$ the bubble nose is blunted, and when $s = 0$ the bubble is spherical. However, the relation between s and σ is unknown. Therefore, Eq. (28) cannot be used to determine terminal velocity. On the other hand, when $\nu = 0$ and the bubble nose is spherical, this formulation yields the Davies-Taylor correlation,

$$U_t = \frac{\sqrt{2}}{3}\sqrt{gd_e} \tag{29}$$

It is observed that for high-Eo simulations, this correlation gives better estimate than that of Fan and Tsuchiya.

3.2. Parameter Setup

The density ratio is the biggest challenge for existing LBMs to simulate two-phase flows because of the compressibility imposed by the LBM. Therefore, incompressible fluids can only be simulated at low density ratios determined by pressure jump at the interface. Although our current model can handle two-phase systems whose density ratio is up to 20, gas–liquid systems encountered in nature are in the range from 1 to 10,000.

Eo can be as high as 10^4, while the upper limit of our model is 10^2. Being limited by the density ratio, large Eo may be achieved by choosing a large bubble diameter or a too-small grid spacing. However, this not only makes computation expensive, it also increases numerical errors. Another way to obtain high Eo is to choose large gravity values, but it should be noted that the LBM is valid only in

Table 1. Parameters for single rising bubble simulations

Case	$\rho l/\rho g$	Eo	Mo	$\|g\|$	ν	τ
1	2.45	5	0.2267	7.75E-05	0.125	0.75
2	2.45	10	0.4535	1.55E-04	0.125	0.75
3	2.45	20	0.9070	3.10E-04	0.125	0.75
4	2.45	40	1.8134	6.20E-04	0.125	0.75
5	2.45	100	4.5350	1.55E-03	0.125	0.75

small-Mach-number simulations. High gravity breaks this limit easily, causing instabilities in the code.

In nature, Mo can go as low as 10^{-12}. Even though our model can simulate such low-Mo flows, the upper limit of Eo has to be lowered. The reason is that, for small-Mo fluids, either surface tension should be high or viscosity should be low. High surface tension leads to small Eo. Although Eo is independent of viscosity, it cannot be set too small either. Since small viscosity increases Re, the possibility of breaking the small-Mach-number assumption is high.

3.3. Test Case and Results

First, a rising bubble in a stationary liquid is studied in a 2-D domain. Table 1 summarizes the parameters used for all the test cases. For all cases, density difference $\Delta\rho$ is set to 0.84. The surface tension is $\sigma = 0.00521$ and the interface thickness is $h = 3.14$, which results in $\alpha = 0.035$ and $\beta = 0.040$. The magnitudes of the gravity and the kinematic viscosity are calculated from Eo and Mo, respectively. Then the relaxation time λ is determined from kinematic viscosity through Eq. (8). Because all the parameters in the simulations are dimensionless, the relaxation parameter, viz., the dimensionless relaxation time $\tau = \lambda/\Delta t$, where Δt is the time step, is displayed in Table 1.

Figures 1 and 2 show the velocity fields and bubble shapes calculated by the LBM and LSM [21]. In these figures, the solid lines represent the interface core, which is assumed to be at $0.5(\rho_l + \rho_g)$ and the zero level-set function in the LBM and LSM, respectively; arrows represent normalized and amplified velocity vectors. The qualitative results, flow pattern and bubble shape, are in excellent agreement with those of the LSM and Takada et al. [11]. It even can be argued that our LBM model is in better agreement with the solutions of the VOF method [11]. Also, bubble shapes predicted by phase-field LBM (Figure 3) are consistent with Clift's bubble shape map.

Another interesting phenomenon related to rising bubble is the vortex structures inside and in the wake region of the bubble. Since measurements in such small-scale experimental studies are challenging, some of these structures are based on velocity and stress continuity assumptions. Those patterns can be found in [18]. For a spherical bubble, our results are consistent with Clift's measurements. However, for a skirt-shaped bubble our model predicts the secondary vortex outside the bubble as different from Clift's speculation.

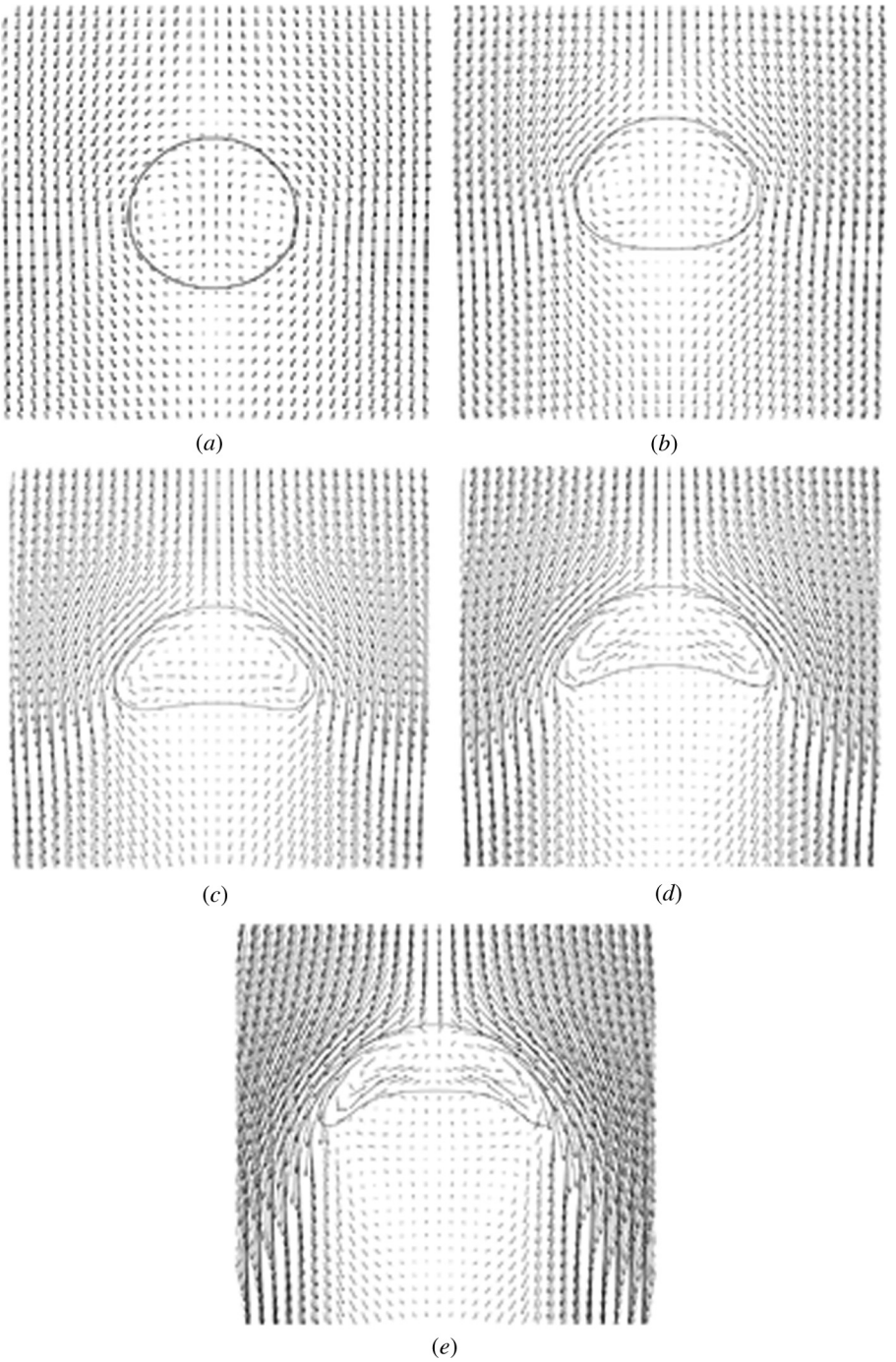

Figure 1. Velocity field around a single bubble which rises in a stationary liquid calculated by the LBM: (*a*) Eo = 5, Mo = 0.2267; (*b*) Eo = 10, Mo = 0.4535; (*c*) Eo = 20, Mo = 0.9070; (*d*) Eo = 40, Mo = 1.8134; (*e*) Eo = 100, Mo = 4.5350.

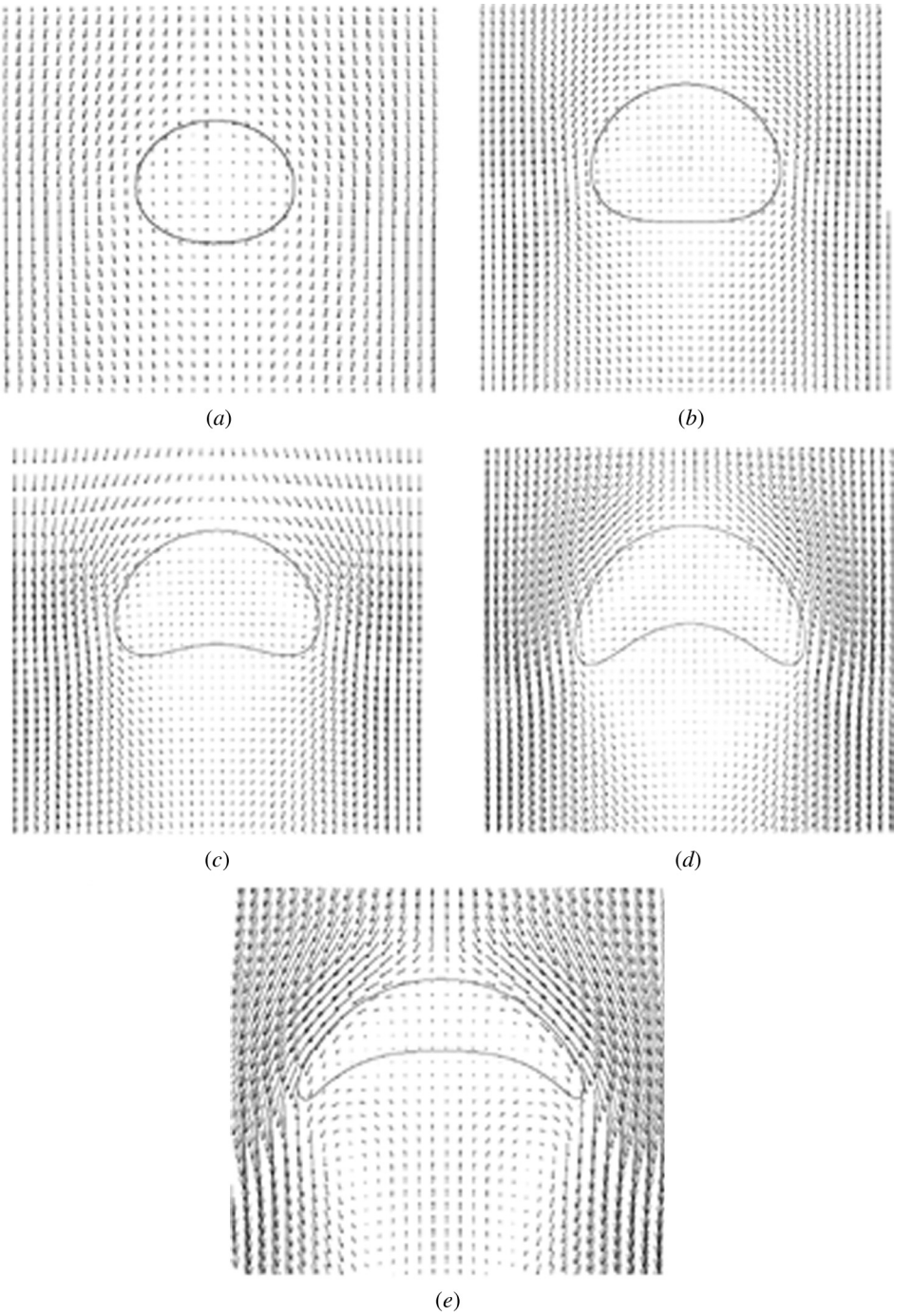

Figure 2. Velocity field around a single bubble which rises in a stationary liquid calculated by the LSM: (*a*) Eo = 5, Mo = 0.2267; (*b*) Eo = 10, Mo = 0.4535; (*c*) Eo = 20, Mo = 0.9070; (*d*) Eo = 40, Mo = 1.8134; (*e*) Eo = 100, Mo = 4.5350.

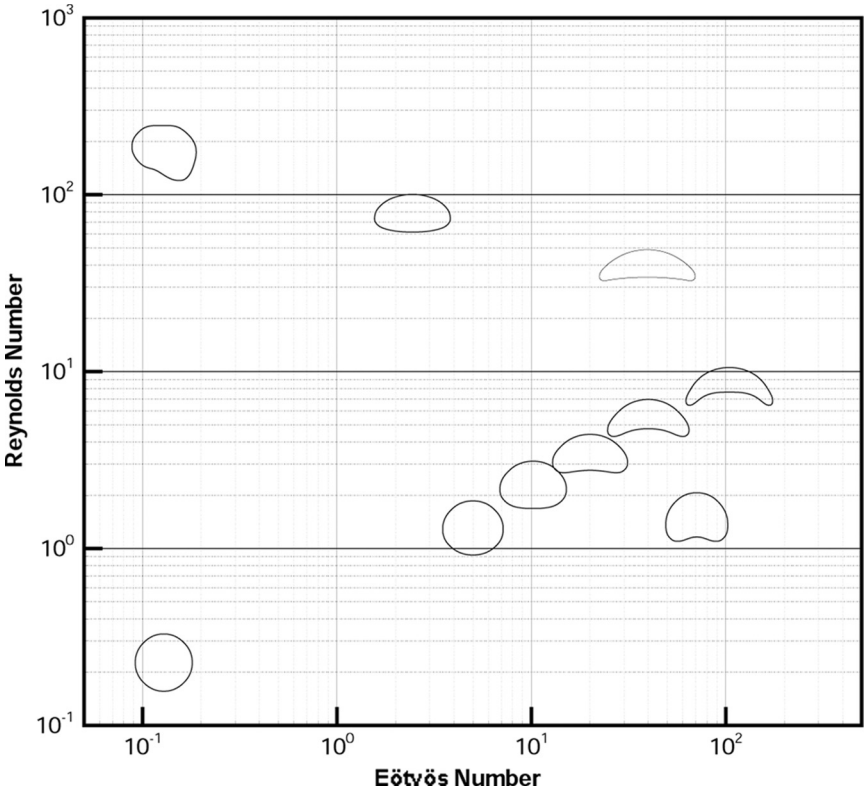

Figure 3. Bubble shape regime map.

3.4. Terminal Velocity

The most important characteristic of a rising bubble is its steady rise velocity, known as terminal velocity. The terminal velocity of a bubble determines the Reynolds number of the flow, and consequently the drag coefficient which quantifies the exact effect of the bubble shape on terminal velocity. Therefore, predicting correct terminal velocities should be the primary goal of two-phase flow models.

In Table 2, the terminal velocities for the five test cases are listed. Also, in this table, the terminal velocities predicted by Takada et al. [11], the LSM of Yue et al. [21], and an empirical equation (26) are given for benchmark purposes. The predicted terminal velocities are in good agreement with the benchmark data.

Because empirical correlations for terminal velocity are valid mostly for spherical or spherical cap-shaped bubbles, our simulations for predicting terminal velocity are also limited by low Eo and Re against skirtlike structures. Figure 4 compares the terminal velocities obtained from our simulations and empirical correlation given by Eqs. (26) and (29). As can be seen, our results are also in good agreement with the empirical correlations. Note that for the chosen Morton numbers, we use Eq. (29) for $\mathrm{Eo} > 10$.

Table 2. Terminal velocities for the test cases

Case	U_t-LBM (this model)	U_t-LBM (Takada)	U_t-VOF (Takada)	U_t-LSM	U_t-Exp (Fan & Tsuhiya)
1	9.00E-3	7.82E-3	8.28E-3	7.70E-3	8.59E-03
2	1.54E-2	1.38E-2	1.43E-2	1.27E-2	1.43E-02
3	2.24E-2	2.17E-2	2.15E-2	1.87E-2	2.33E-02
4	3.19E-2	3.11E-2	3.08E-2	2.70E-2	3.75E-02
5	5.43E-2	5.03E-2	5.05E-2	4.00E-2	6.86E-02

3.5. 3-D Rising Bubble Simulations

Furthermore, we repeat some 2-D bubble simulations using 3-D phase-field LBM. Use of symmetric boundary conditions permits us to achieve approximately the same resolution as 2-D simulations. However, due to computational cost, we simulate only two selected cases, Case 3 and Case 5. The results, which are shown in Figures 5 and 6, validate the 2-D bubble rising results both qualitatively and quantitatively.

Figure 7 compares wake structure of 2-D and 3-D rising bubble simulations. Since surface tension in 3-D simulations depends on two orthogonal directions in the surface, 2-D and 3-D simulations present a little difference. Axisymmetric flow causes a shorter wake region than the one in the 2-D simulation. Also, the vortex in the wake region is closer to the edge of the bubble skirt in 3-D simulation because of slightly different skirt structure.

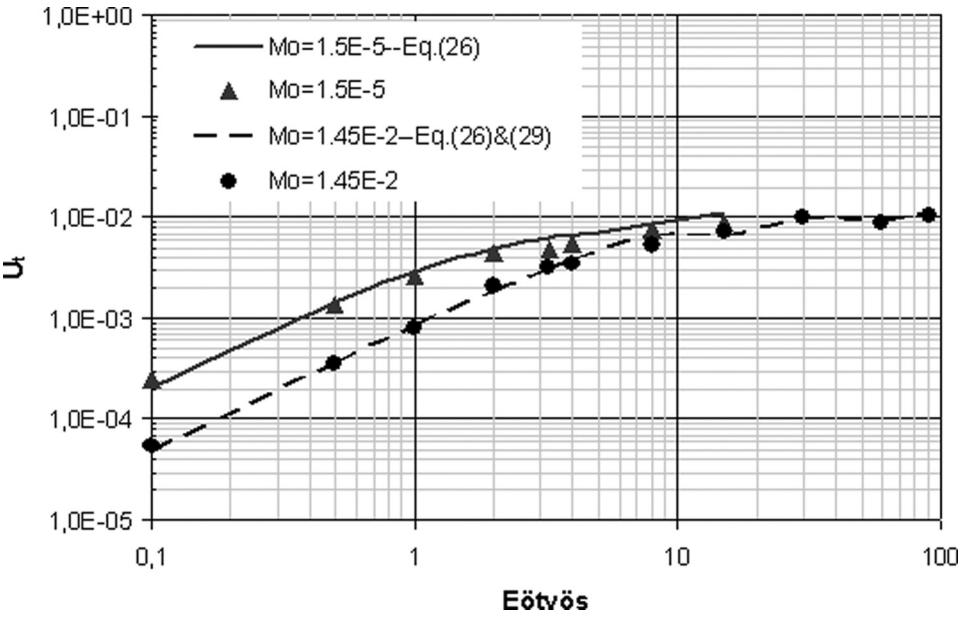

Figure 4. Eötvös number versus terminal velocity.

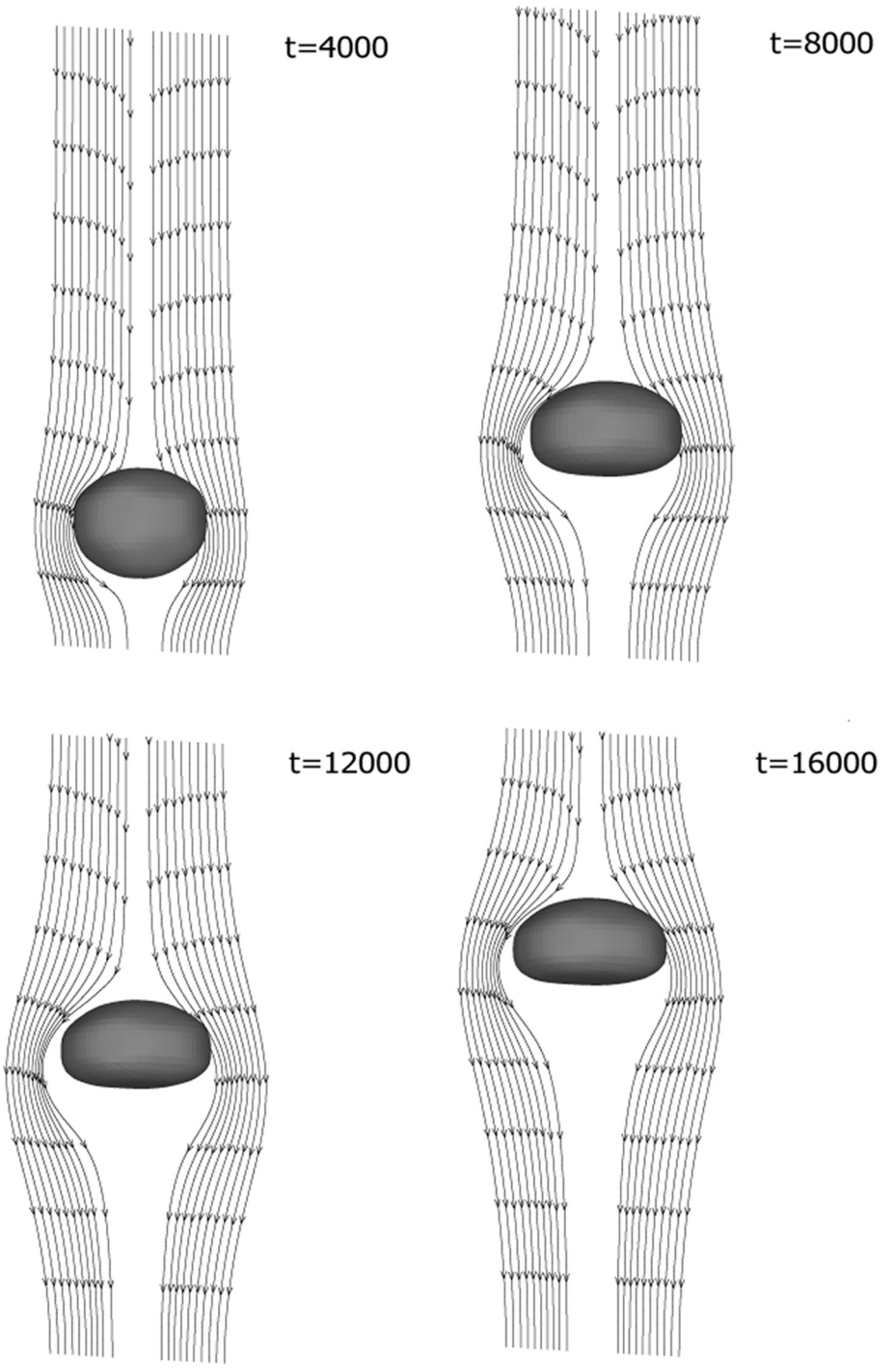

Figure 5. 3-D rising bubble for Case 3 with the streamlines in the center plane.

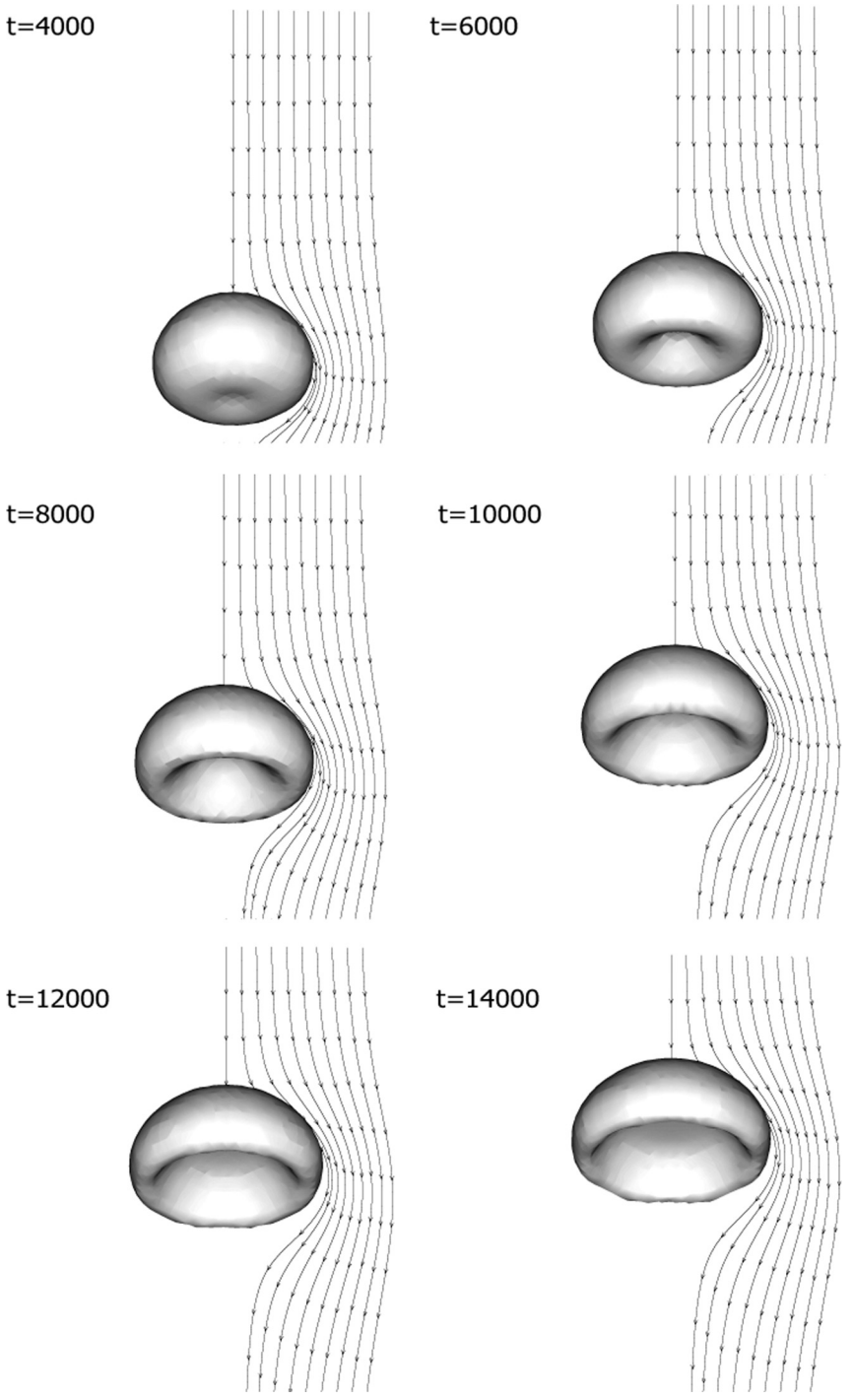

Figure 6. 3-D rising bubble for Case 5 with the streamlines in the center plane.

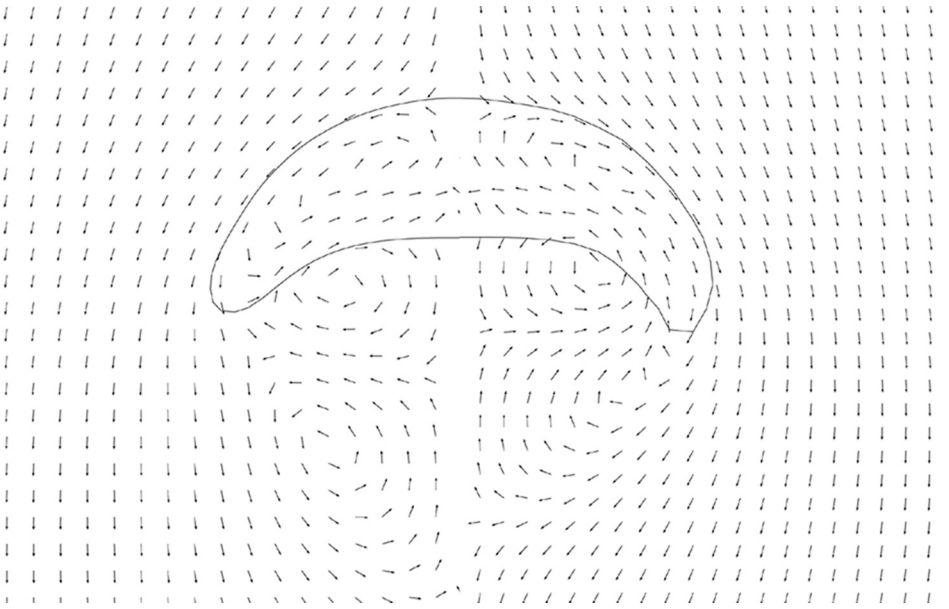

Figure 7. Comparison of wake structure between 2-D and 3-D rising bubble for Case 5, on left-hand side and right-hand side, respectively.

3.6. Drag Coefficient

Another important characteristic parameter is drag coefficient, C_D, because the bubble equivalent diameter–terminal velocity relation is preferably expressed in terms of C_D–Re. Since these parameters are independent of surface tension force, fluid properties or bubble shape should be taken into account, thus presenting the relationship between them. For example, at large Eo and Mo, a bubble may have a spherical cap shape even though Re is sufficiently small (Re < 200). Bhaga and Weber [22] identified a critical Mo, which is 4×10^{-3}, to make a distinction between high- and low-Mo liquids. According to them, while high-Mo fluids decrease monotonically, low-Mo liquids have a minimum C_D.

For high-Mo liquid simulations we use the following empirical formula:

$$C_D = \left[(2.67)^{0.9} + \left(\frac{16}{\mathrm{Re}} \right)^{0.9} \right]^{1/0.9} \tag{30}$$

The corresponding curve is shown with a solid line in Figure 8.

For low-Mo liquids, no correlation is presented for spherical cap bubbles. Therefore, we can only present a comparison with the experimental studies in the Stokes flow regimes. We use the following equation:

$$C_D = \frac{16}{\mathrm{Re}} \qquad \text{for Re} < 2 \tag{31}$$

$$C_D = \frac{14.9}{\mathrm{Re}^{0.78}} \qquad \text{for Re} > 2 \tag{32}$$

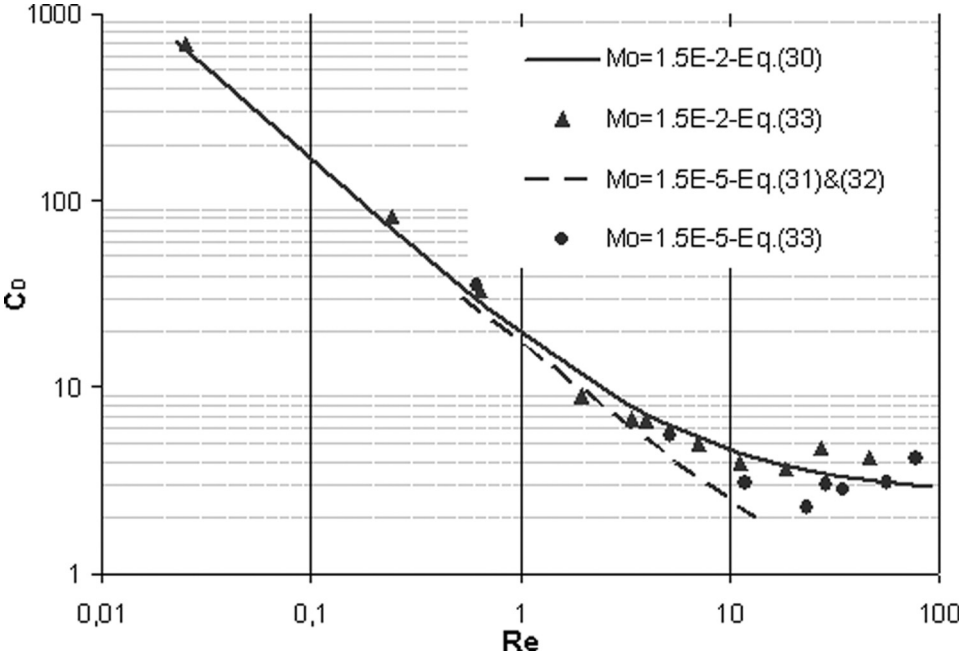

Figure 8. Reynolds number versus drag coefficient. Solid and broken lines represent empirical correlations, and the symbols show our results.

To compare our results with the above empirical formulation, the bubble drag coefficient is calculated by

$$C_D = \frac{F}{\frac{1}{2} U_t^2 D} \tag{33}$$

where F is the force applied by the fluid on the bubble, U_t is the terminal velocity, and D is the bubble equivalent diameter. Although the force experienced by the bubble is composed of normal viscous stress and pressure, we neglect the normal viscous stress and use buoyancy force. In the literature, the bubble equivalent diameter is defined as a sphere diameter with the same volume as the bubble. Since bubble volume is approximately preserved, D is the initial diameter of our circular bubble.

A series of simulations for a low Mo and a high Mo have been conducted, and the results are displayed in Figure 8. At low Reynolds number ($\mathrm{Re} < 5$), bubble deformation is small and drag coefficient is almost independent of Morton number. For higher-Re simulation ($\mathrm{Re} > 10$), deformation becomes considerably high. Then the viscous effects change the structure of the vortices in the wake region. Therefore, for low-Mo fluids, drag coefficient behaves differently than for high-Mo fluids, creating a minimum at a certain Reynolds number. For example, the results show that this minimum is around $\mathrm{Re} \approx 30$ for a fluid whose $\mathrm{Mo} = 1.5 \times 10^{-5}$. The reason for this behavior of different fluids is the bubble shape and its wake region. While the bubbles in high-Mo fluids develop spherical caps with closed wake or skirted with

smooth steady skirt with increasing terminal velocity, the bubbles in low-Mo fluids transform from oblate ellipsoidal shape to spherical cap with open unsteady wake. During this transition, drag coefficient of the bubble reaches a local minimum.

4. CONCLUSION

A new, two-component, immiscible LBM based on the phase-field method is employed for single rising bubble simulations. The results are qualitatively and quantitatively compared with experimental and numerical studies, and good agreement between them is found over a wide range of flow regimes. Consequently, the phase-field LBM method can accurately predict single-bubble dynamics and physics of interface advection.

Additionally, numerical experiments show that secondary vortices actually develop in the wake region of the bubble, unlike Clift's speculation. This observation is also confirmed by 3-D rising bubble simulations. Furthermore, behavior of a single rising bubble in low-Mo and high-Mo fluids has been studied, and change of drag coefficient with Morton number is proved numerically by the phase-field LBM.

REFERENCES

1. J. A. Sethian and P. Smereka, Level Set Methods for Fluid Interfaces, *Annu. Rev. Fluid Mech.*, vol. 35, pp. 341–372, 2003.
2. T. Lee and C.-L. Lin, Rarefaction and Compressibility Effects of the Lattice Boltzmann Equation Method in a Gas Microchannel, *Phys. Rev. E*, vol. 71, pp. 1–10, 2005.
3. S. Succi, *The Lattice Boltzmann Equation for Fluid Flow and Beyond*, Clarendon Press, Oxford, UK, 2001.
4. H. Chen, S. Kandasamy, S. Orszag, R. Shock, S. Succi, and V. Yakhot, Extended Boltzmann Kinetic Equation for Turbulent Flows, *Science*, vol. 301, pp. 633–636, 2003.
5. X. Shan and H. Chen, Lattice Boltzmann Model for Simulating Flows with Multiple Phases and Components, *Phys. Rev. E*, vol. 47, no. 3, pp. 1815–1819, 1993.
6. M. Swift, W. Osborne, and J. Yeomans, Lattice Boltzmann Simulations of Non-ideal Fluids, *Phys. Rev. Lett.*, vol. 75, pp. 830–833, 1995.
7. D. J. Holdych, J. G. Georgiadis, and R. O. Buckius, Migration of a van der Waals Bubble: Lattice Boltzmann Formulation, *Phys. Fluids*, vol. 13, p. 817, 2001.
8. X. He, X. Shan, and G. D. Doolen, Discrete Boltzmann Equation Model for Nonideal Gases, *Phys. Rev. E*, vol. 57, no. 1, pp. R13–R16, 1998.
9. L. Luo, A Unified Theory of Non Ideal Gas Lattice Boltzmann Models, *Phys. Rev. Lett.*, vol. 81, no. 8, pp. 1618–1621, 1998.
10. R. Zhang, X. He, G. D. Doolen, and S. Chen, Surface Tension Effects on Two-Dimensional Two-Phase Kelvin-Helmholtz Instabilities, *Adv. Water Resources*, vol. 24, pp. 461–478, 2001.
11. N. Takada, M. Misawa, A. Tomiyama, and S. Fujiwara, Numerical Simulation of Two- and Three-Dimensional Two-Phase Fluid Motion by Lattice Boltzmann Method, *Comput. Phys. Commun.*, vol. 129, pp. 233–246, 2000.
12. K. Sankaranarayanan, X. Shan, I. G. Kevrekidis, and S. Sundaresan, Analysis of Drag and Virtual Mass Forces in Bubbly Suspensions Using an Implicit Formulation of the Lattice Boltzmann Method, *J. Fluid Mech.*, vol. 452, pp. 61–96, 2002.
13. D. Jacqmin, Calculation of Two-Phase Navier-Stokes Flows Using Phase-Field Modelling, *J. Comput. Phys.*, vol. 155, no. 1, pp. 96–127, 1999.

14. D. M. Anderson, G. B. McFadden, and A. A. Wheeler, Diffuse-Interface Methods in Fluid Mechanics, *Annu. Rev. Fluid Mech.*, vol. 30, pp. 139–165, 1998.
15. J. W. Cahn and J. E. Hilliard, Free Energy of a Nonuniform System. III. Nucleation in a Two-Component Incompressible Fluid, *J. Chem. Phys.*, vol. 31, pp. 688–699, 1959.
16. X. He, S. Chen, and R. Zhang, A Lattice Boltzmann Scheme for Incompressible Multiphase Flow and Its Application in Simulation of Rayleigh-Taylor Instability, *J. Comput. Phys.*, vol. 152, pp. 642–663, 1999.
17. T. Lee and C.-L. Lin, A Stable Discretization of the Lattice Boltzmann Equation for Simulation of Incompressible Two-Phase Flows at High Density Ratio, *J. Comput. Phys.*, vol. 206, pp. 16–47, 2005.
18. R. Clift, J. R. Grace, and M. E. Weber, *Bubbles, Drops, and Particles*, Academic Press, New York, 1978.
19. L.-S. Fan and K. Tsuchiya, *Bubble Wake Dynamics in Liquids and Liquid-Solid Suspensions*, Butterworth-Heinemann, Boston, 1990.
20. D. D. Joseph, Rise Velocity of a Spherical Cap Bubble, *J. Fluid Mech.*, Vol. 488, pp. 213–223, 2003.
21. W. Yue, C.-L. Lin, and V. C. Patel, Numerical Simulation of Unsteady Multidimensional Free Surface Motions by Level Set Method, *Int. J. Numer. Meth. Fluids*, vol. 42, no. 8, pp. 853–884, 2003.
22. T. Bhaga and M. Weber, Bubbles in Viscous Liquids; Shapes, Wakes and Velocities, *J. Fluid Mech.*, vol. 105, pp. 61–85, 1981.